DOI: 10.65731/ama/2026-0038

EFFECTIVE ELASTIC MODULI OF THIN FILMS WITH ROUGH SURFACES: A MODELING APPROACH

Taras NAHIRNYJ[*], **Michał SĄSIADEK**[*], **Kostiantyn TCHERVINKA**[**]

[*]Institute of Mechanical Engineering, University of Zielona Gora, 4 Szafrana, Zielona Gora, 65-516, Poland
[**]Faculty of Mechanics and Mathematics, Ivan Franko National University of Lviv, 1, Universytetska St., Lviv, 79000, Ukraine

T.Nahirnyj@gmail.com, M.Sasiadek@iim.uz.zgora.pl, K.Tchervinka@gmail.com

received 24 February 2026, revised 29 March 2026, accepted 11 April 2026

Abstract: The governing system of equations for the model of a locally inhomogeneous elastic body is based on constitutive equations generalized to account for local inhomogeneity of the binding energy and includes an equation for the mass density in the form of an inhomogeneous Helmholtz equation. This paper shows that, by selecting appropriate mass sources (the inhomogeneous term in the mass density equation), it is possible to obtain a mass density distribution in the near-surface region that reflects the characteristics of the Abbott–Firestone curve, which is widely used in engineering practice to describe surface roughness. Using a flat surface as an example, the influence of the model parameters on the core, peak, and valley zones of the material ratio curve is investigated. When modeling the influence of the surface roughness parameters of a real body on the effective elastic moduli of thin films, it is assumed that the local Young's modulus and Poisson's ratio are functions of the mass density. The solution to the problem for a stretched layer is expressed in quadratures, and its analysis is performed using numerical methods. In particular, it is shown that the characteristic length scales of the size effects of the effective elastic moduli depend on the structural heterogeneity of the material and on the sizes of the core, peak, and valley zones of the roughness profile.

Key words: mathematical modeling, bearing ratio curve, size effects, thin films

1. INTRODUCTION

In engineering practice, thin films and thin-film elements have found widespread application [1-4]. In these elements, surface and bulk factors contribute comparably to their overall energy. Particles located on the surface of a body experience interactions only from the internal regions, whereas particles in the deeper layers of the body interact isotropically in all directions. This implies that the binding energy of a particle changes as one moves from the surface into the bulk of the material. Such inhomogeneity results in a non-zero stress-strain state, which is sometimes accounted for by incorporating surface energy effects into the model [5-9]. Properly accounting for near-surface inhomogeneity allows for the description of various size-dependent effects, including surface stresses and mechanical strength. The binding energy within a material is closely related to its mass density, and near-surface inhomogeneity can be linked to surface roughness. In a single-component solid body, variations in mass density inhomogeneity are typically correlated with changes in porosity.

Geometric inhomogeneity is an inherent characteristic of every real surface, regardless of its formation or processing method. To quantify surface roughness, various numerical parameters are used, distinguishing between the surface's three-dimensional description and its profile's two-dimensional representation. A key parameter in surface profiling is the bearing area curve, known as the Abbott-Firestone curve or material ratio curve. Originally developed to analyze the contact between two surfaces, this curve illustrates the relationship between the actual contact area and the separation distance of the surfaces [10, 11]. When a surface is depicted through a profilometric contour, the Abbott-Firestone curve, as a function of height z, represents the fraction of the nominal area contained within the surface contour at elevation z. In other words, it quantifies the percentage of space occupied by the material at a given height within the real surface profile.

Figure 1 illustrates the key features of the curve along with the Rk family parameters. Here, R_t represents the total height of the roughness profile, defined as the distance between its highest peak and lowest valley. R_k represents the thickness of the core zone. The parameters Mr_1 and Mr_2 are percentage values that characterize the core zone, usually with $Mr_2 = 80\%$ and $Mr_1 = 5\%$ or 10%. Parameters R_{pk} and R_{vk} correspond to the average heights of the peaks above and the valleys below the core zone, respectively. Note, lower R_{pk} values indicate higher abrasion resistance and an increased contact area, whereas higher R_{vk} values suggest an improved capacity of the surface to retain lubricant.

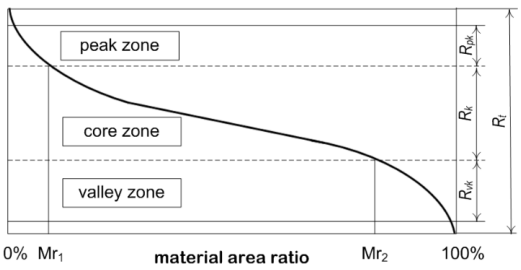

Fig. 1. An Abbott-Firestone curve illustrating the peak, valley and core zones of the surface roughness profile and R_k family of parameters

The curve is typically used in manufacturing and quality control for tribology and wear analysis, as well as for evaluating lubrication performance [12, 13]. It is determined experimentally based on a profilometer scan of the surface, which generates a surface height profile. Its physical significance is related to the concept of mass density since the portion of space occupied by the material corresponds to the mass density of a porous material.

If the Abbott-Firestone curve is plotted as mass density ρ versus distance r measured from the highest point of the surface profile to the depth of the body, it will resemble the representation shown in Fig. 2. Here ρ_* represents the mass density of a solid medium of the identical material. This means that the microinhomogeneities of a real body's surface are characterized by near-surface mass density inhomogeneity within a continuum description, where the surface of the body is modeled as a smooth geometric surface (e.g. a plane) passing through the highest peak of the actual surface. In classical solid mechanics, mass density is typically assumed to be constant throughout the entire body and for a given material, it does not vary from point to point.

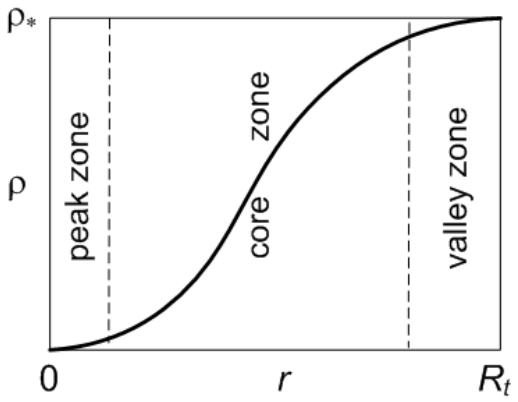

Fig. 2. Abbott-Firestone curve in terms of mass density ρ

Near-surface mass density inhomogeneity and the effects related to the inhomogeneity of binding energy can be addressed within the framework of the local-gradient approach in thermomechanics [14-16]. In the study [17], a mathematical model of a locally inhomogeneous elastic body considering surface roughness was proposed. One of the equations of this model is the equation for mass density. Its solution for a body with flat boundaries reflects the regularities of the bearing ratio curve.

Considering the variation in mass density from point to point, an accurate description must account for the corresponding change in material properties including elastic characteristics such as the moduli of elasticity. In porous solids, Young's modulus E and Poisson's ratio ν are often related to the porosity coefficient ϕ by the following relationships

$$E = E_*(1-\phi), \quad \nu = \nu_*(1-\phi) \tag{1}$$

Here, quantities intrinsic to the fully dense (non-porous) material (in the reference state) are denoted by an asterisk. These dependencies are widely reported in literature and are supported both experimentally [18-20] and theoretically, particularly through homogenization methods [21-23]. Since porosity reflects the amount of void space in a material, these relationships can also be expressed in terms of mass density:

$$E = E_* \frac{\rho}{\rho_*}, \quad \nu = \nu_* \frac{\rho}{\rho_*} \tag{2}$$

This is especially important in thin films, where the size of the near-surface mass density inhomogeneity region can be comparable to the thickness of the body. It is also worth noting that, knowing the dependencies of Young's modulus and Poisson's ratio on density, one can, if necessary, derive similar relationships for other elastic moduli.

The objective of this work is to model and analyze how the surface roughness of a real body affects the elastic moduli in thin films. This study is conducted within the model of a locally inhomogeneous elastic body with surface roughness. In addition, it is investigated how the thickness of the near-surface region of mass density inhomogeneity, especially the regions of peaks and valleys, depends on the model parameters.

2. BASIC RELATIONS OF LOCAL GRADIENT APPROACH IN MECHANICS OF ELASTIC SOLIDS

One of the key equations of the locally inhomogeneous elastic body model is the equation for mass density [14, 17]

$$\nabla^2\rho - \xi_m^2(\rho - \rho_*) = -\xi_m^2 d_{sm} \tag{3}$$

Here ξ_m is a parameter that characterizes the material structure of the body, d_{sm} is a function accounting for the method of surface formation (referred to as mass sources for convenience), $\nabla^2 = \vec{\nabla}\cdot\vec{\nabla}$, where $\vec{\nabla}$ is the del operator, and "$\cdot$" stands for the dot product. It should be noted that mass sources allow us to consider the inhomogeneity of mass density in a region whose size differs significantly from the characteristic grain size of the material, which the parameter ξ_m is usually associated with [14]. When describing near-surface heterogeneity, it is reasonable to assume that the function d_{sm} decreases to zero as it extends from the surface into the depth of the body.

In the paper [17], mass sources were proposed for bodies with nominally flat boundaries to account for the patterns of the bearing area curve. The parameters of these mass sources enable control over the size of near-surface heterogeneity regions, as well as the dimensions of peaks and valleys zones.

In the model of a locally inhomogeneous elastic body, the complete system of equations includes the equation (3) for mass density, along with the equations governing the elastic fields — specifically, those for the displacement vector and the stress or strain tensors.

The linearized equilibrium equation for the displacement vector $\vec{u}$ and mass density ρ takes the form

$$(1-2\nu)\nabla^2\vec{u} + \vec{\nabla}\left(\vec{\nabla}\cdot\vec{u}\right) - 2a_m(1+\nu)\vec{\nabla}\rho = 0 \tag{4}$$

where a_m is a material parameter.

Choosing the stress tensor $\hat{\sigma}$ as the solving function, instead of the displacement vector $\vec{u}$, results in another system of equations for the model. For this case, equation (4) should be replaced with the following two equations

$$\vec{\nabla}\cdot\hat{\sigma} = 0,$$

$$\vec{\nabla}\times\left\{\vec{\nabla}\times\left[(1+\nu)\hat{\sigma} - \left(\nu\sigma - Ea_m(\rho-\rho_*)\right)\hat{I}\right]\right\}^T = 0 \tag{5}$$

Here $\sigma = \hat{\sigma}:\hat{I}$, $\hat{I}$ is the second order identity tensor, the symbols ":" and "×" denotes double inner and cross products respectively, the superscript T indicates transposition.

It is worth noting that the parameter conjugated to ρ is the thermodynamic chemical potential H, and the perturbation of the latter

DOI: 10.65731/ama/2026-0038

is associated with the perturbation of the binding energy [14, 15]. We also note that the stress tensor $\hat{\sigma}$ and the thermodynamic chemical potential H are related to the strain tensor $\hat{e}$ and the mass density ρ by the relations

$$\hat{\sigma} = \frac{E}{1+\nu}\hat{e} + \frac{E}{1-2\nu}\left(\frac{\nu}{1+\nu}e - a_m(\rho-\rho_*)\right)\hat{I}$$

$$H = H_* - \frac{E}{1-2\nu}a_m e + a_{mm}(\rho-\rho_*) \quad (6)$$

and the strain tensor $\hat{e}$ is related to the displacement vector $\vec{u}$ by the Cauchy relation

$$\hat{e} = \frac{1}{2}\left[\vec{\nabla}\otimes\vec{u} + \left(\vec{\nabla}\otimes\vec{u}\right)^T\right] \quad (7)$$

Here a_{mm} is a material parameter, H_* is the thermodynamic chemical potential of the material in the reference state, $e = \hat{e}:\hat{I}$, $\otimes$ stands for the tensor product.

When formulating boundary value problems, the systems of equations (3), (4) or (3), (5) must be supplemented with an expression for d_{sm} and the appropriate boundary conditions.

3. INTERFACE INHOMOGENEITY NEAR A NOMINALLY FLAT BOUNDARY

Let us consider an isotropic deformable half-space free from external force loading, occupying the domain $x \geq 0$ in the rectangular Cartesian coordinate system $\{x, y, z\}$. The reference state is taken to be the state of a homogeneous body, with constant mass density equal to ρ_*. We assume that the surface of the body passes through the highest vertex of the profile of the real surface, therefore, we take the following boundary condition together with the condition of the mass density being bounded at infinity

$$\rho(0) = 0, \quad \lim_{x\to+\infty}\rho(x) = \rho_* \quad (8)$$

The choice of the mass density at the surface of a body depends on various factors, including the modeling approach and the state of the surface. A method for justifying the determination of surface density is discussed in [24], which arrives at a value of $\rho_*/2$ for a perfectly flat surface, with lower values for rougher surfaces. In general, the density at the surface of the solid can vary from 0 to ρ_*. In this study, we rely on the Abbott-Firestone curve, which represents the percentage of space occupied by the material. We observe that at the boundary of the solid, this percentage starts from zero. Therefore, we assume that the density at the surface of the solid is zero.

Assuming that d_{sm} depends only on the coordinate x, the solution of equation (3), that satisfies conditions (8) can be written as:

$$\rho(x) = \rho_*(1-\exp(-\xi_m x)) + \frac{1}{2}\xi_m \exp(\xi_m x)\times$$
$$\times\int_x^{+\infty} d_{sm}(t)\exp(-\xi_m t)\,dt - \frac{1}{2}\xi_m\exp(-\xi_m x)\times \quad (9)$$
$$\times\left[\int_0^{+\infty} d_{sm}(t)\exp(-\xi_m t)\,dt - \int_0^x d_{sm}(t)\exp(\xi_m t)\,dt\right]$$

In [17], the expression for the mass sources d_{sm} was adopted as follows

$$d_{sm}(x) = -\rho_*[a\exp(-(\xi_s x)^k) + b\exp(-\xi_{sd}x)]$$
$$a + b = 1 \quad (10)$$

where a, b, k, ξ_s, ξ_{sd} are constant parameters. It is also shown that this representation allows considering the regularities of the material ratio curve into the mass density distribution, including the existence of peak, core and valley zones. This is illustrated in particular by the graphs in Fig. 3 which present the dependence of ρ/ρ_* on $\xi_m x$. In Fig. 3 *a*) $a = 1, \xi_s/\xi_m = 0.1, k = 6{,}3{,}1$ (blue, red and green curves); in Fig. 3 *b*) $a = 0.8$, $\xi_{sd}/\xi_m = 0.08$, $\xi_s/\xi_m = 0.1$, $k = 6{,}3{,}1$ (curves 1–3); in Fig. 3*c*) $a = 0.8$, $\xi_{sd}/\xi_m = 0.08, k = 6, \xi_s/\xi_m = 0.8{,}0.4{,}0.2{,}0.1$ (curves 1–4). For $k > 1$ and $a = 1$, the figures exhibit a clearly pronounced peak region. For $k > 1$ and $a < 1$, the peak region becomes apparent at smaller values of ξ_s/ξ_m (Fig. 3 *c*).

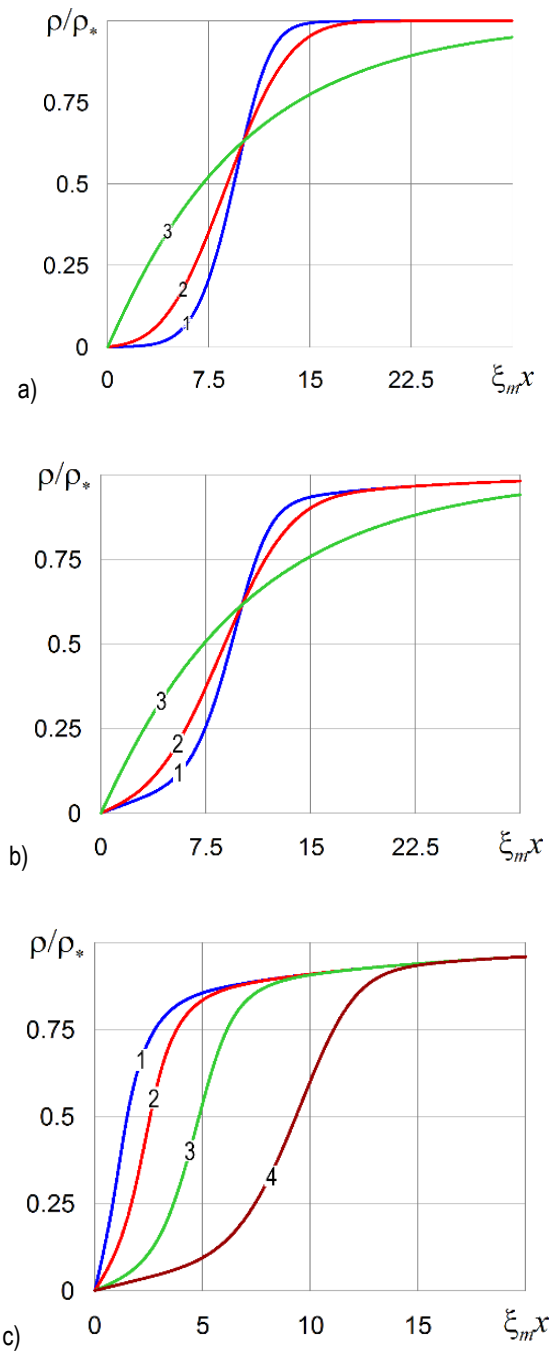

Fig. 3. Interface inhomogeneity of mass density near a flat boundary

The demarcation lines between the core zone and the peak/valley zones are defined by the values of Mr_1 and Mr_2. We assume that core zone starts where $\rho/\rho_* = 0.10$ and ends where

$\rho/\rho_* = 0.80$. Additionally in numerical investigation we assume that $\rho(R_t)/\rho_* = 0.99$.

Figs. 4-6 show the effect of mass source parameters on the thicknesses of the near-surface mass density inhomogeneity zone S_{Rt}, peak zone S_{PZ} and valley zone S_{VZ}.

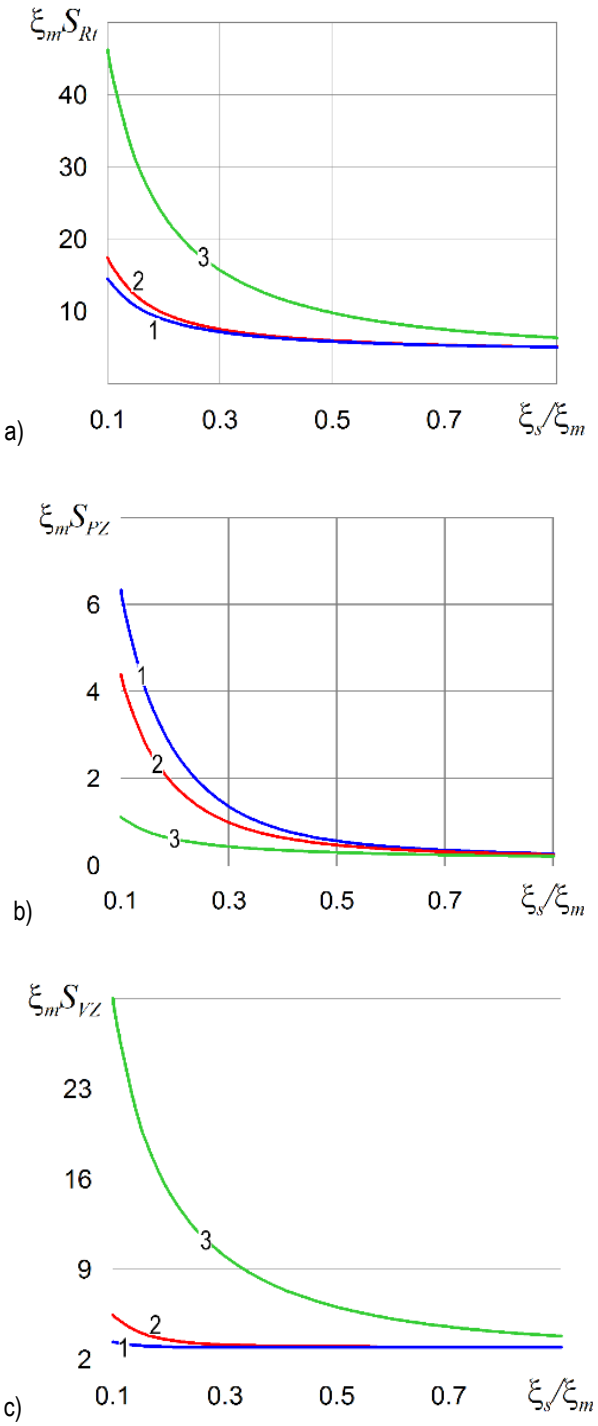

Fig. 4. The influence of the parameter ξ_s/ξ_m on S_{Rt}, S_{PZ}, S_{VZ}. $a = 1$, $k = 6,3,1$ – curves 1–3 respectively

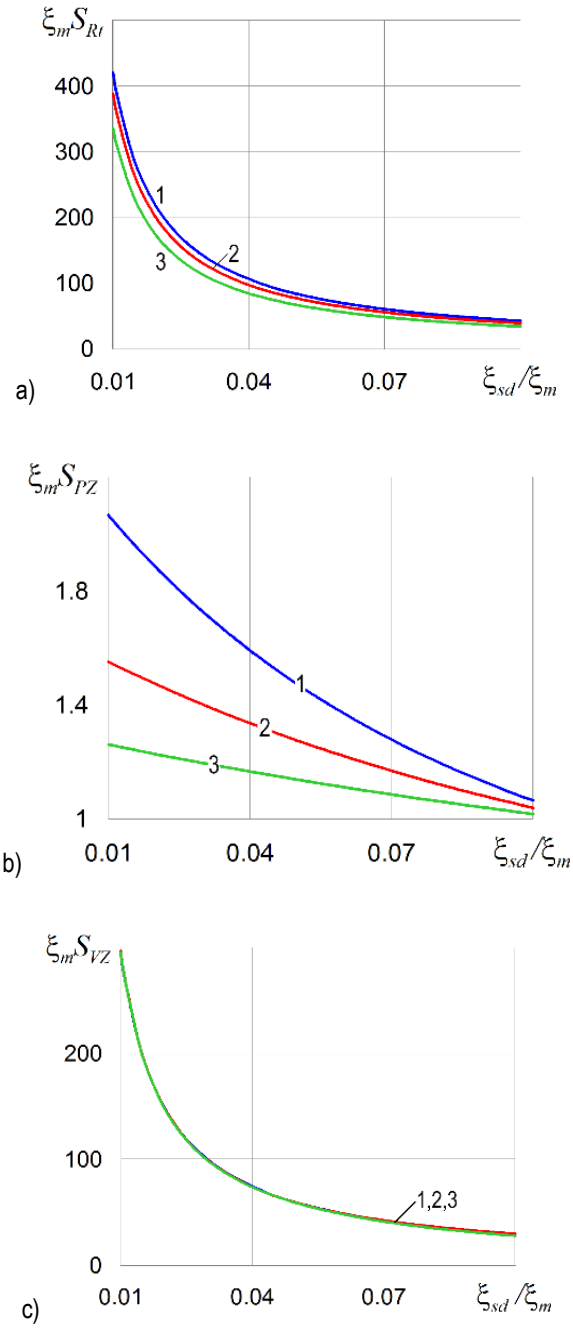

Fig. 5. The influence of the parameter ξ_{sd}/ξ_m on S_{Rt}, S_{PZ}, S_{VZ}. $k = 3$, $\xi_s/\xi_m = 0.3$, $a = 0.3,0.5,0.7$ – curves 1–3 respectively

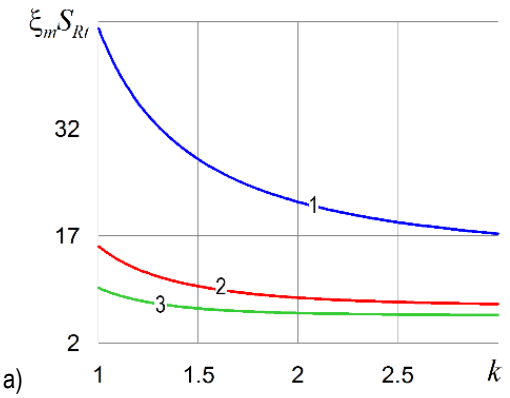

DOI: 10.65731/ama/2026-0038

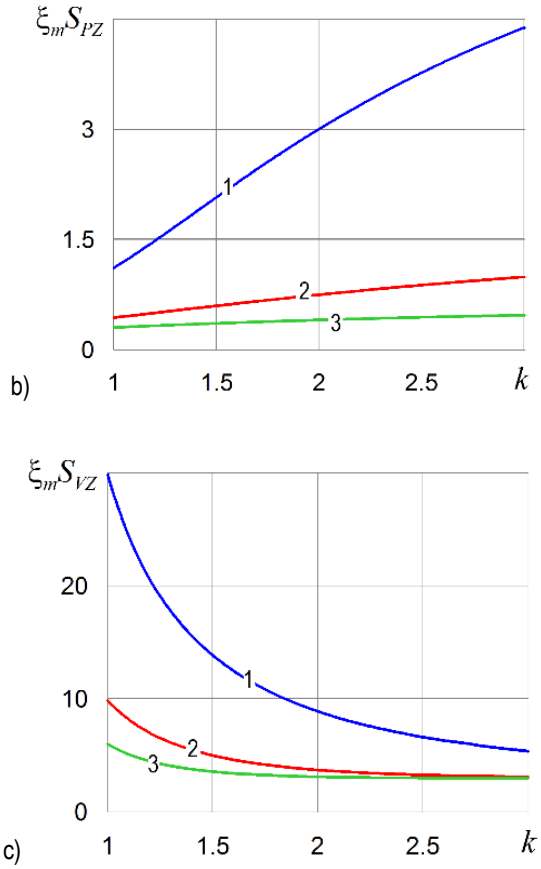

Fig. 6. The influence of the parameter k on S_{Rt}, S_{PZ}, S_{VZ}. $a = 1$, $\xi_s/\xi_m = 0.1, 0.3, 0.5$ – curves 1–3 respectively

The graphs presented above demonstrate the significant potential for modeling the material curves of real surfaces using the parameters of the mass density sources. It is important to note that the parameter k enables the model to capture the peak zone, while the second term in the expression for the mass sources (10) provides effective control over the extent of the valley zone.

4. ELASTIC MODULI DEPENDENT ON MASS DENSITY

Generalizing formulas (2) for Young's modulus and Poisson's ratio, we assume

$$E = E_*\left(\frac{\rho}{\rho_*}\right)^{\beta_E} \equiv E_* f_E(\rho)$$

$$\nu = \nu_*\left(1 - \beta_\nu\left(1 - \frac{\rho}{\rho_*}\right)\right) \equiv \nu_* \varphi_\nu(\rho) \tag{11}$$

Here E_*, ν_* are Young's modulus and Poisson's ratio of the body material in the reference state, β_E, β_ν are the constants. This is consistent with the literature, including [19, 25, 26].

Since mass density varies from point to point, the elastic moduli exhibit the same property. These moduli are referred to as *local elastic moduli*. On the other hand, Young's modulus is an experimentally measurable characteristic of a body, defined as the ratio of the applied external force intensity to the resulting relative elongation of the body (specifically, the elongation of its surface) caused by the load. The measured value represents the average over the cross-sectional area of the sample. We denote this as E^{ef}, referring to it as the *effective Young's modulus*. The same considerations apply to the *effective Poisson's ratio* ν^{ef}. A significant number of studies have been devoted to the investigation of effective moduli in heterogeneous bodies, including [27].

Using the example of a layer, we examine how the roughness of the body's real surface affects the effective elastic moduli.

5. THE STEADY STATE OF THE STRETCHED LAYER

Consider an isotropic solid layer, which occupies the region $|x| \le l$ in the rectangular Cartesian coordinate system $\{x, y, z\}$. We assume that on the surfaces of the layer $x = l, x = -l$, which are identical, the mass density is equal to 0 and at $y \to \pm\infty$ the force load of constant intensity σ_a acts along the Oy axis.

Under such an external action, a one-dimensional situation over x variable is realized in the body

$$\hat{\sigma} = \hat{\sigma}(x), \quad \rho = \rho(x).$$

The steady state of the layer is described by the system of equations

$$\frac{d\sigma_{xx}}{dx} = 0$$

$$\frac{d^2}{dx^2}\left(\frac{1+\nu}{E}\sigma_{\gamma\gamma} - \frac{\nu}{E}\sigma\right) = -\frac{d^2}{dx^2}\left(a_m(\rho - \rho_*)\right),\ \gamma = \{y, z\}$$

$$\frac{d^2\rho}{dx^2} - \xi_m^2(\rho - \rho_*) = -\xi_m^2 d_{sm}, \tag{12}$$

boundary conditions

$$\rho = 0, \quad \sigma_{xx} = 0 \tag{13}$$

at surfaces $x = l, x = -l$ and conditions

$$\int_{-l}^{l}\sigma_{yy}\,dx = 2l\sigma_a, \int_{-l}^{l}\sigma_{zz}\,dx = 0,$$

$$\int_{-l}^{l} x\sigma_{yy}\,dx = 0, \int_{-l}^{l} x\sigma_{zz}\,dx = 0 \tag{14}$$

in arbitrary layer cross sections *y = const*, *z = const*.

We will conduct a numerical investigation for the function d_{sm} given by the formula

$$d_{sm} = -\rho_*\left\{a\left[\exp\left(-\left(\xi_s(l+x)\right)^k\right) + \exp\left(-\left(\xi_s(l-x)\right)^k\right)\right] + b\frac{\cosh(\xi_{sd}x)}{\cosh(\xi_{sd}l)}\right\},\quad a + b = 1 \tag{15}$$

Additionally, we assume $(\xi_s l)^k \gg 1$. It can be noted that if we consider the density distribution close to the surface $x = -l$ of a thick layer, this formula is consistent with equation (10).

The solution of the formulated problem (11)-(15) written for the mass density and non-zero components of the stress tensor reads

$$\rho(x) = \rho_* + \xi_m\int_0^x d_{sm}(t)\sinh\left(\xi_m(t-x)\right)dt + \\ + \frac{\cosh(\xi_m x)}{\cosh(\xi_m l)}\left[-\rho_* + \xi_m\int_0^l d_{sm}(t)\sinh\left(\xi_m(l-t)\right)dt\right]$$

$$\sigma_{yy}(x) = \frac{f_E(\rho(x))\sigma_a}{2\left(1+\nu_*\varphi_\nu(\rho(x))\right)}\frac{1}{In_2}\left(\frac{1+\nu_*\varphi_\nu(\rho(x))}{1-\nu_*\varphi_\nu(\rho(x))} + \frac{In_1}{In_2}\right) - \\ - \frac{E_*\rho_* a_m f_E(\rho(x))}{1-\nu_*\varphi_\nu(\rho(x))}\left(\frac{\rho(x)}{\rho_*} - 1 - \frac{In_1}{In_2}\right)$$

$$\sigma_{zz}(x) = \frac{f_E(\rho(x))\sigma_a}{2\left(1+\nu_0\varphi_\nu(\rho(x))\right)}\frac{1}{In_2}\left(\frac{1+\nu_0\varphi_\nu(\rho(x))}{1-\nu_0\varphi_\nu(\rho(x))} - \frac{In_2}{In_0}\right) - \\ - \frac{E_*\varrho_* a_m f_E(\rho(x))}{1-\nu_*\varphi_\nu(\rho(x))}\left(\frac{\rho(x)}{\rho_*} - 1 - \frac{In_1}{In_2}\right) \tag{16}$$

where

$$In_0 = \frac{1}{2l}\int_{-l}^{l} \frac{f_E(\rho(x))}{1+\nu_*\varphi_\nu(\rho(x))}\,dx$$

$$In_1 = \frac{1}{2l}\int_{-l}^{l} \frac{f_E(\rho(x))}{1-\nu_*\varphi_\nu(\rho(x))}\left(\frac{\rho(x)}{\rho_*}-1\right)\,dx$$

$$In_2 = \frac{1}{2l}\int_{-l}^{l} \frac{f_E(\rho(x))}{1-\nu_*\varphi_\nu(\rho(x))}\,dx$$

6. EFFECTIVE YOUNG'S MODULUS AND POISSON'S RATIO

Based on the state equation (6) for the strain tensor we write

$$\hat{e} = \frac{1+\nu}{E}\hat{\sigma} - \frac{\nu}{E}\sigma\hat{I} + a_m(\rho-\rho_*)\hat{I} \tag{17}$$

Using the solution (16), for normal components of the strain tensor we obtain

$$e_{xx}(x) = -\frac{\nu_*\varphi_\nu(\rho(x))}{1-\nu_*\varphi_\nu(\rho(x))}\frac{\sigma_a}{E_*In_2} + \frac{1+\nu_*\varphi_\nu(\rho(x))}{1-\nu_*\varphi_\nu(\rho(x))}\times$$

$$\times\, a_m(\rho(x)-\rho_*) - 2\nu_* a_m \frac{\varphi_\nu(\rho(x))}{1-\nu_*\varphi_\nu(\rho(x))}\frac{In_1}{In_2}$$

$$e_{yy}(x) = \frac{\sigma_a}{2E_*In_2}\left(1+\frac{In_2}{In_0}\right) + a_m\rho_*\frac{In_1}{In_2}$$

$$e_{zz}(x) = \frac{\sigma_a}{2E_*In_2}\left(1-\frac{In_2}{In_0}\right) + a_m\rho_*\frac{In_1}{In_2} \tag{18}$$

This means that the component e_{yy}^* of the strain e_{yy} caused by external force load is

$$e_{yy}^* = \frac{\sigma_a}{2E_*In_2}\left(1+\frac{In_2}{In_0}\right) \tag{19}$$

Thus, for the effective Young's modulus E^{ef} we can write the formula

$$E^{ef} = 2E_*\frac{In_0In_2}{In_0+In_2} \tag{20}$$

Poisson's ratio is a measure of the body size change in the transverse direction for tensile-compressive stress. Using the obtained solution and the state equation, for the component $e_{xx}^{(\sigma_a)}$ of strain e_{xx} caused by an external force load, we obtain

$$e_{xx}^{(\sigma_a)} = -\frac{\nu_*\varphi_\nu(\rho(x))}{1-\nu_*\varphi_\nu(\rho(x))}\frac{\sigma_a}{E_0In_2} \tag{21}$$

Integrating this expression over the width of the layer, we determine the average deformation e_{xx}^* caused by the force load

$$e_{xx}^* = -\frac{\sigma_a}{E_*}\frac{In_3}{In_2} \tag{22}$$

where

$$In_3 = \frac{\nu_*}{2l}\int_{-l}^{l}\frac{\varphi_\nu(\rho(x))}{1-\nu_*\varphi_\nu(\rho(x))}\,dx$$

According to the definition of the Poisson's ratio, using formulas (19), (22) for ν^{ef} we write

$$\nu^{ef} = 2\frac{In_0In_3}{In_0+In_2} \tag{23}$$

The effective elastic moduli E^{ef}/E_* and ν^{ef}/ν_* dependence on the layer thickness (parameter $\xi_m l$) is shown respectively in Fig. 7 *a*) and Fig. 7 *b*) for $\nu_* = 0.33$, $k = 2$, $\xi_s/\xi_m = 0.8; 0.2$ (curves 1,2), $\xi_{sd}/\xi_m = 0.08$, $\beta_E = 1$, $\beta_\nu = 0.5$, $a = 0.5$ (solid lines), $a = 1$ (dashed lines). The curve 3 corresponds to $a = 1$, $\xi_s/\xi_m = 0.2$, $\beta_E = 1$, $\beta_\nu = 0.5$, $k = 1$. As the layer thickness increases, the value of effective elastic moduli tends toward E_*, ν_*. This indicates the presence of a size effect. Considering the third term in formula (15), which increases the valley zone, may lead to a significant change in the value of the effective elastic moduli. This effect is more pronounced in films with smaller thickness. Additionally, the analysis of the solution suggests that including this term increases the number of characteristic values of size effects.

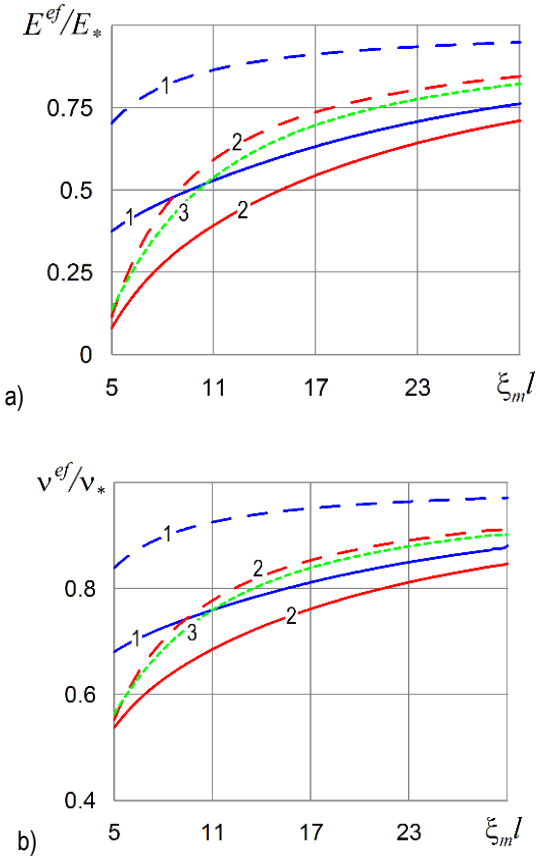

Fig. 7. Size effect of effective elastic moduli E^{ef}, ν^{ef}

The reduction of the parameter ξ_{sd} corresponds to an increase in the valley zone as one can see from Fig. 5*c*. As the valley zone expands, the value of the effective elastic moduli E^{ef}, ν^{ef} decreases. This is illustrated by the graphs in Fig. 8 for the following parameters: $\nu_* = 0.33$, $\xi_m l = 20$, $k = 2$, $\xi_s/\xi_m = 0.2; 0.4; 0.8$ (curves 1–3), $a = 0.5$, $\beta_E = 1$, $\beta_\nu = 0.5$.

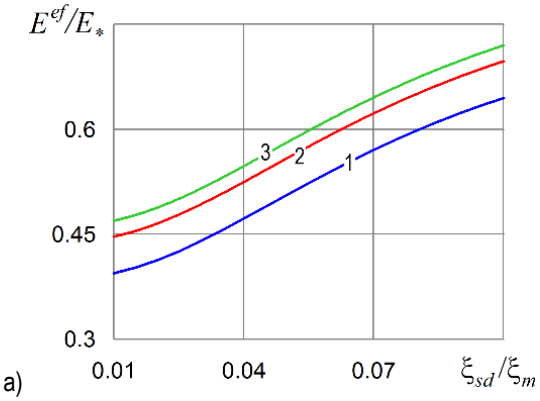

DOI: 10.65731/ama/2026-0038

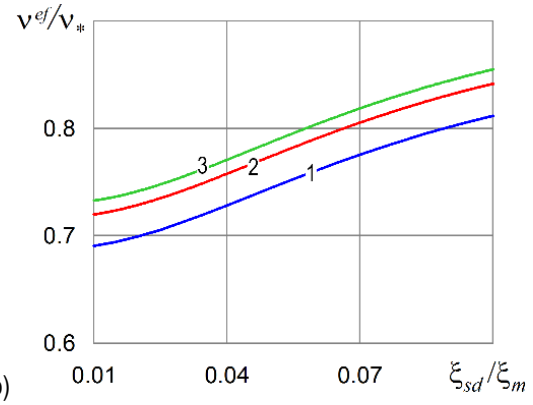

Fig. 8. Dependence of the effective elastic moduli E^{ef}, ν^{ef} on the parameter ξ_{sd}/ξ_m

The graphs in Figure 3 *c*) indicate that in the region $k > 1$, with a decrease in the value of ξ_s, the thickness of the peak zone increases. An increase in ξ_s leads to an increase in the effective elastic moduli E^{ef}, ν^{ef} for films of constant thickness. This is illustrated by the graphs in Fig. 9, which show the dependence of E^{ef}/E_*, ν^{ef}/ν_* on the parameter ξ_s/ξ_m for $\nu_* = 0.33$, $\xi_m l = 20{,}10$ (red and blue lines), $k = 2$, $\xi_{sd}/\xi_m = 0.08$, $\beta_E = 1$, $\beta_\nu = 0.5$, $a = 0.5$ (solid lines), $a = 1$ (dashed lines). The line 3 corresponds to $\xi_m l = 10$, $a = 1$, $\xi_s/\xi_m = 0.2$, $\beta_E = 1$, $\beta_\nu = 0.5$, $k = 1$.

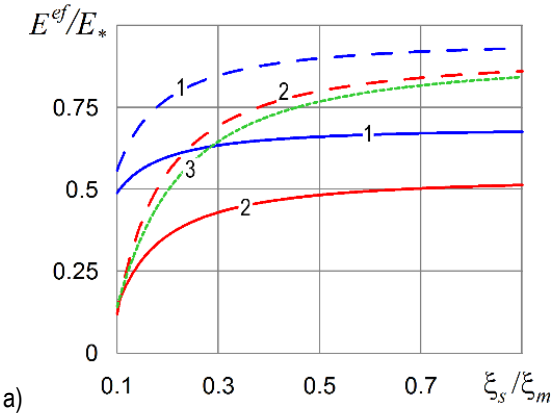

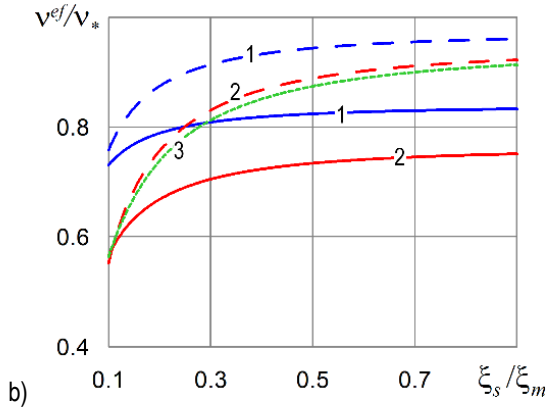

Fig. 9. Dependence of the effective elastic moduli E^{ef}, ν^{ef} on the parameter ξ_s/ξ_m

As the parameter k increases, the Young's modulus and Poison ratio values slightly increase. This is illustrated by the graphs in Fig. 10 for $\nu_* = 0.33$, $\xi_m l = 10, 15, 20$ (curves 1–3), $\xi_{sd}/\xi_m = 0.08$, $\beta_\nu = 0.5$, $\beta_E = 1$, $a = 0.5$.

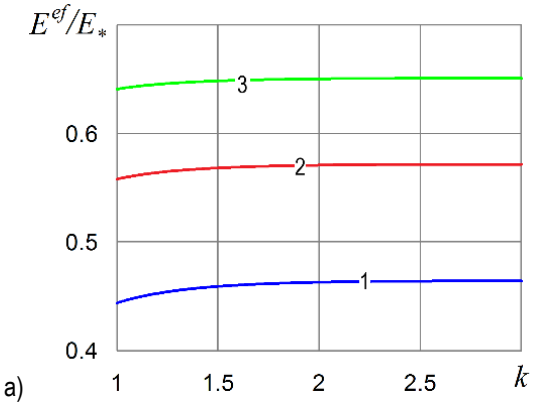

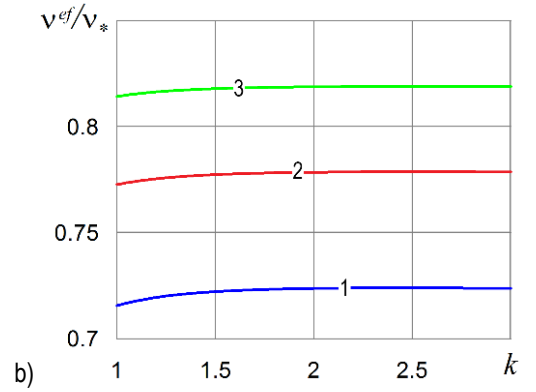

Fig. 10. Dependence of the effective elastic moduli E^{ef}, ν^{ef} on the parameter k

The dependence of moduli E^{ef}, ν^{ef} on the parameters β_E and β_ν is shown respectively on Fig. 11 and Fig. 12 for $\nu_* = 0.33$, $\xi_m l = 20{,}10$ (curves 1,2), $k = 2$, $\xi_s/\xi_m = 0.3$, $\xi_{sd}/\xi_m = 0.08$, $a = 0.5$ (solid lines), $a = 1$ (dashed lines). The curve 3 corresponds $\xi_m l = 10$, $k = 1$. On Fig. 11 $\beta_\nu = 0.5$ and on Fig. 12 $\beta_E = 1$. We note the practically linear dependence of ν^{ef} on β_ν, as well as the weak dependence of E_{ef} on β_ν and ν^{ef} on β_E.

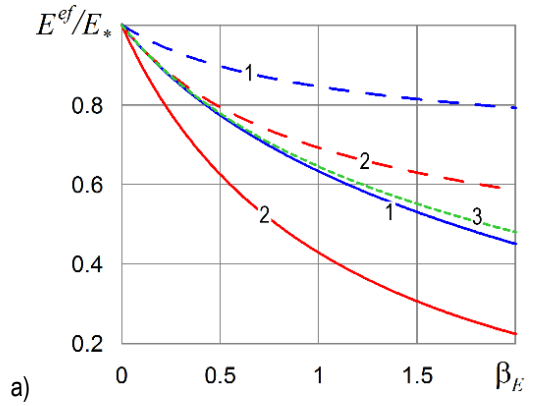

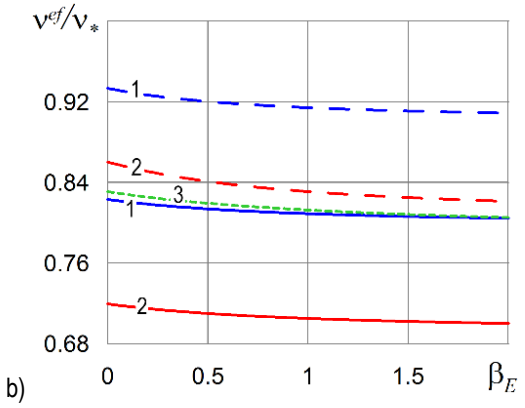

Fig. 11. Dependence of the effective elastic moduli E^{ef}, ν^{ef} on the parameter β_E

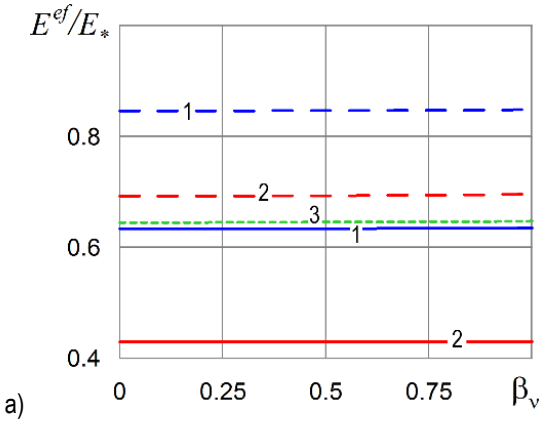

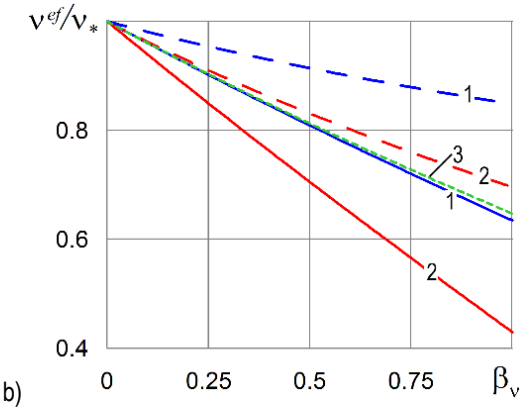

Fig. 12. Dependence of the effective elastic moduli E^{ef}, ν^{ef} on the parameter β_ν

7. CONCLUSION

The Abbott-Firestone curve (bearing ratio curve) is widely used in engineering practice to describe the surface texture of solid bodies. Therefore, solid mechanics models that account for surface roughness should accurately capture the characteristics of this curve. Models that incorporate the characteristics of the material curve include those developed within the locally gradient approach in thermomechanics. One of the equations in these models is the equation for mass density. In a locally inhomogeneous elastic body, the mass density equation takes the form of an inhomogeneous Helmholtz equation. When considering the roughness of the real surface of the body, the inhomogeneous term of this equation, the so-called mass sources, is selected so that the distribution of mass density reflects the distribution and regularities of the material curve. Numerical results indicate that adjusting mass source parameters allows for effective control over the mass density distribution near a nominally flat surface, as well as the sizes of the core, peak, and valley zones. Thus, by appropriately selecting mass source parameters, the profile of a real rough surface can be accurately simulated.

The effective elastic moduli, experimentally measured for thin films, reflect the properties of a real rough surface. They exhibit a size effect, meaning their value increases monotonically with film thickness, approaching the values of a medium made of identical material. The characteristic scales of these size effects depend on the material's structural heterogeneity and the sizes of the core zone, zones of peaks and valleys in the roughness profile. For thin films, the values of the effective Young's modulus E^{ef} and Poisson's ratio ν^{ef} significantly depend on the parameters of the mass sources. Any alteration in the latter, specifically, a change in the rough surface characteristics, necessitates a refinement of the effective moduli values. We note that ν^{ef} exhibits a weak dependence on β_E, while E^{ef} shows a weak dependence on β_ν —parameters that characterize how the local Young's modulus and local Poisson's ratio vary with density, respectively.

Further research is needed to evaluate the approximations used in describing the material ratio curve, particularly the implications of neglecting the peak zone. This issue is closely related to the choice of body surface location in continuum mechanics models.

REFERENCES

1. Abadias G, Chason E, Keckes J, Sebastiani M, Thompson GB, Barthel E, Martinu L. Review Article: Stress in thin films and coatings: current status, challenges, and prospects. J Vac Sci Technol A. 2018;36(2): 020801. https://doi.org/10.1116/1.5011790
2. Bull SJ, Chalker PR, Johnston C, Moore V. The effect of roughness on the friction and wear of diamond thin films. Surf Coat Technol. 1994; 68:603–610. https://doi.org/10.1016/0257-8972(94)90224-0
3. Elanjeitsenni VP, Vadivu KS, Prasanth BM. A review on thin films, conducting polymers as sensor devices. Mater Res Express. 2022;9(2):022001. https://doi.org/10.1088/2053-1591/ac4aa1
4. Pang X, Zhang L, Yang H, Gao K, Volinsky AA. Residual stress and surface energy of sputtered TiN films. J Mater Eng Perform. 2015;24:1185–1191. https://doi.org/10.1007/s11665-015-1393-5
5. Fahs A, Mi S, Nicolazzi W, Molnár G, Bousseksou A. Disentangling surface energy and surface/interface stress effects in spin crossover nanomaterials. Adv Phys Res. 2023;2(10):2200055. https://doi.org/10.1002/ apxr.202200055
6. Goudarzi T., Avazmohammadi R, Naghdabadi R. Surface energy effects on the yield strength of nanoporous materials containing nanoscale cylindrical voids. Mech Mater. 2010;42(9):852-862. https://doi.org/10.1016/j.mechmat.2010.07.006
7. Ling FF, Lai WM, Lucca DA. Fundamentals of Surface Mechanics. New York: Springer; 2002. https://doi.org/10.1007/978-0-387-21776-5
8. Nasr Esfahani M, Jabbari M. Influence of the surface stress on the size-dependent elastic behavior of silicon nanowires. J Appl Phys. 2020;127(19):195106. https://doi.org/10.1063/5.0006989
9. Povstenko Y. Mathematical modeling of phenomena caused by surface stresses in solids. In: Altenbach H, Morozov N, editors. Surface Effects in Solid Mechanics. Berlin Heidelberg: Springer. Adv Struc Mater. 2013; 30. https://doi.org/10.1007/978-3-642-35783-1_11
10. Johnson KL. Contact Mechanics. Cambridge: Cambridge University Press; 1985. https://doi.org/10.1017/CBO9781139171731
11. Kragelsky IV, Demkin NB. Contact area of rough surfaces. Wear. 1960;3(3):170–187. https://doi.org/10.1016/0043-1648(60)90136-8

DOI: 10.65731/ama/2026-0038

12. Sedlaček M, Podgornik B, Vižintin J. Correlation between standard roughness parameters skewness and kurtosis and tribological behaviour of contact surfaces. Tribol Int. 2012;48:102–112. https://doi.org/10.1016/j.triboint.2011.11.008
13. Zhu S, Huang P. Influence mechanism of morphological parameters on tribological behaviors based on bearing ratio curve. Tribol Int. 2017;109:10–18. https://doi.org/10.1016/j.triboint.2016.12.014
14. Nahirnyj T, Tchervinka K. Mathematical modeling of structural and nearsurface non-homogeneities in thermoelastic thin films. Int J Eng Sci. 2015;91:49–62. https://doi.org/10.1016/j.ijengsci.2015.02.001
15. Nahirnyj T, Tchervinka K. Functional kinetic equations in mathematical modeling of coupled processes in solids. Contin Mech Thermodyn. 2020;32:1727–1743. https://doi.org/10.1007/s00161-020-00877-1
16. Nahirnyj T, Tchervinka K. Mathematical modeling of the coupled processes in nanoporous bodies. Acta Mech Autom. 2018;12(3):196–203. https://doi.org/10.2478/ama-2018-0030
17. Nahirnyj T, Sąsiadek M, Tchervinka K. Modeling the effect of surface roughness on mechanical fields in an elastic solid bounded by nominally flat surfaces. Int J Solids Struct. 2024;302:112979. https://doi.org/10.1016/j.ijsolstr.2024.112979
18. Asmani M, Kermel C, Leriche A, Ourak M. Influence of porosity on Young's modulus and Poisson's ratio in alumina ceramics. J Eur Ceram Soc. 2001;21(8):1081–1086. https://doi.org/10.1016/S0955-2219(00)00314-9
19. Kováčik J. Correlation between Young's modulus and porosity in porous materials. J Mater Sci Lett. 1999;18(13):1007–1010. https://doi.org/10.1023/A:1006669914946
20. Lam DC, Lange FF, Evans AG. Mechanical properties of partially dense alumina produced from powder compacts. J Am Cer Soc. 1994;77(8):2113–2117. https://doi.org/10.1111/j.1151-2916.1994.tb07105.x
21. Altenbach H. An alternative determination of transverse shear stiffnesses for sandwich and laminated plates. Int J Solids Struct. 2000;37(25):3503–3520. https://doi.org/10.1016/S0020-7683(99)00057-8
22. Jankowski P. On the nonlocal interaction range for stability of nanobeams with nonlinear distribution of material properties. Acta Mech Autom. 2022;16(2): 151-161. https://doi.org/10.2478/ama-2022-0019
23. Bîrsan M, Sadowski T, Marsavina L, Linul E, Pietras D. Mechanical behavior of sandwich composite beams made of foams and functionally graded materials. Int J Solids Struct. 2013;50(3-4):519–530. https://doi.org/10.1016/j.ijsolstr.2012.10.011
24. Nahirnyj T, Tchervinka K. Near-surface mass defect in models of locally heterogeneous solid mechanics. Acta Mech Autom. 2019;13(3):205-210. https://doi.org/10.2478/ama-2019-0027
25. Gibson LJ, Ashby MF. Cellular Solids: Structure and Properties. Cambridge: Cambridge University Press; 1999. https://doi.org/10.1017/CBO978 1139878326
26. Niyogi S, Gupta BS. Mechanical properties and pore size distribution in athermal shear-strained porous glasses. arXiv [Preprint] arXiv:2106.03473. 2021. https://doi.org/10.48550/arXiv.2106.03473
27. Altenbach H, Bruno G, Eremeyev VA, Gutkin MY, Müller WH, editors. Mechanics of Heterogeneous Materials. Cham: Springer International Publishing; 2023. https://doi.org/10.1007/978-3-031-28744-2

Taras Nahirnyj: https://orcid.org/0000-0001-5118-6827

Michał Sąsiadek: https://orcid.org/0000-0002-7804-9459

Kostiantyn Tchervinka: https://orcid.org/0000-0002-2466-072X